



**HAL**  
open science

# Robust Contact and Friction Model for the Fatigue Estimate of a Wire Rope in the Mooring Line of a Floating Offshore Wind Turbine

Federico Bussolati, Pierre-Alain Guidault, Martin Guiton, Olivier Allix, Peter Wriggers

► **To cite this version:**

Federico Bussolati, Pierre-Alain Guidault, Martin Guiton, Olivier Allix, Peter Wriggers. Robust Contact and Friction Model for the Fatigue Estimate of a Wire Rope in the Mooring Line of a Floating Offshore Wind Turbine. *Virtual Design and Validation*, 93, Springer, pp.249-270, 2020, Lecture Notes in Applied and Computational Mechanics, 9783030381554. 10.1007/978-3-030-38156-1\_13. hal-02541704

**HAL Id: hal-02541704**

**<https://hal.science/hal-02541704>**

Submitted on 21 Oct 2023

**HAL** is a multi-disciplinary open access archive for the deposit and dissemination of scientific research documents, whether they are published or not. The documents may come from teaching and research institutions in France or abroad, or from public or private research centers.

L'archive ouverte pluridisciplinaire **HAL**, est destinée au dépôt et à la diffusion de documents scientifiques de niveau recherche, publiés ou non, émanant des établissements d'enseignement et de recherche français ou étrangers, des laboratoires publics ou privés.

# Robust Contact and Friction Model for the Fatigue Estimate of a Wire Rope in the Mooring Line of a Floating Offshore Wind Turbine

F. Bussolati, P.-A. Guidault, M. L. E. Guiton, O. Allix and P. Wriggers

**Abstract** Station keeping of Floating Wind Turbine (FOWT) is ensured by mooring lines. They may be composed of steel wire ropes, which are particularly difficult to design against the Fatigue Limit State, because the standard Tension-Tension rules cannot capture accurately the influence of the frictional contact interactions between the wires when the rope is bent. We propose here a new model linking the tension and curvature time series computed by a global scale model to a micro-scale model simulating the fretting fatigue at an inter-wire contact location. This new model of a detailed part of rope relies on the use of a new contact element, which allows to gain robustness and CPU time. This is of crucial importance for the large number of simulations required by a fatigue life estimate. A case study is presented considering a FOWT equipped with three pairs of catenary mooring lines. The computed tension and curvature obtained for a severe sea state are transferred to the detailed model of the wire rope, with periodic boundary conditions representing the rope continuity. The time series of sliding and contact forces are finally reported at different locations within the rope, providing possible input data for a fretting fatigue analysis.

---

F. Bussolati (✉) · P.-A. Guidault · O. Allix  
LMT, ENS Paris-Saclay, CNRS, Université Paris-Saclay, 61 Avenue du Président Wilson,  
94230 Cachan Cedex, France  
e-mail: [bussolati@ens-paris-saclay.fr](mailto:bussolati@ens-paris-saclay.fr); [federico.bussolati@ifpen.fr](mailto:federico.bussolati@ifpen.fr)

P.-A. Guidault  
e-mail: [guidault@ens-paris-saclay.fr](mailto:guidault@ens-paris-saclay.fr)

O. Allix  
e-mail: [allix@ens-paris-saclay.fr](mailto:allix@ens-paris-saclay.fr)

F. Bussolati · M. L. E. Guiton  
IFP Energies nouvelles - Direction Physico-chimie et Mécanique appliquée, Rond-point de  
l'échangeur de Solaize, 69360 Solaize, France  
e-mail: [martin.guiton@ifpen.fr](mailto:martin.guiton@ifpen.fr)

P. Wriggers  
LUH - Leibniz Universität Hannover [Hannover] 44961 - Gottfried Wilhelm Leibniz Universität  
Hannover Welfengarten 1, 30167 Hannover, Germany  
e-mail: [wriggers@ikm.uni-hannover.de](mailto:wriggers@ikm.uni-hannover.de)

# 1 Introduction

Floating Offshore Wind Turbines (FOWT) have been developed in recent years, to participate to the energy transition challenge. Similarly to any floating structure, their station keeping relies on mooring lines anchored to the seabed. The mooring lines can be constituted by chains, steel wire ropes and synthetic rope. Synthetic ropes have been proposed very recently in FOWT applications, while wire ropes have been extensively employed in the oil and gas industry for many decades. They indeed offer a large tensile strength, with considerable less weight than chains. Even if they have been extensively studied, the wire rope fatigue is still difficult to estimate when they are exposed to free bending [1]. Indeed, many studies [2, 3] show that bending contribution may reduce dramatically the fatigue life of the component. This effect is linked to fretting contact interactions at the wire scale, with crack initiations located near the wire rope neutral axis where the slidings are the largest [3, 4]. Such phenomena are not taken into account in the usual tension-tension fatigue laws of the design standards (e.g. [5]) which could contribute to explain the high number of mooring failures reported by oil and gas industry [6].

Some analytical models have been developed in order to characterize the wire interactions and the mechanical properties of a wire rope. In [7, 8] each wire layer is modeled as an orthotropic cylinder, while in [9–11] wires are considered as curved beams.

In more recent years, researchers developed Finite Element models of wire ropes, employing 3D solid [12, 13] or beam elements [14]. However, wire ropes used in offshore mooring systems have large diameters, typically greater than 50 mm, which limits the interest of 3D solid elements models because of a too large CPU time. In [14], a first way to reduce this computational cost is proposed with the use of beam elements. The mechanical behavior of a multi-layer wire rope is reproduced with an acceptable approximation, as demonstrated by the results of a tension-bending test. Such models rely on many publications which have been devoted to the specific case of beam-to-beam contact [15] then extended to friction [16], generalized to include possible rectangular sections [17, 18]. Recent work in this domain have also proposed alternative formulations improving the geometric accuracy. For instance, [19] and [20, 21] can take into account the rotation interaction between the contact beams, with a parametrization based on the Frenet-Serret basis for the prior and convected coordinates for the latters. Also, [22] uses an intermediary integrating surface which contributes to smooth the functional for Newton algorithm.

In this paper we propose a new contact and friction model which offers a considerably larger time saving by exploiting the small inter-wire sliding [23, 24]. The potential of this model is demonstrated by applying it to the same FOWT study case than in [25]. It is composed of a semi-submersible floater supporting a 3.6 MW downsized version of the NREL 5 MW wind turbine and equipped with catenary mooring lines. We follow here the same methodology used in [25], with the following differences.

- The contact kinematics is enriched here by additional sliding terms along the circumferences of the wire beam elements.
- The initialization of the loading considers here the bending before the tension, in order to reduce the tangential contact force influence.
- The lay angle of the internal wire layer is greater.
- Kinematic coupling relations within the detailed wire rope model have been eliminated as it has been recognized to introduce numerical artifacts. They were added in order to impose the correct kinematics to a reference wire at each layer, but actually in [23] it is shown that they are not needed.

## 2 Detailed Wire Rope Model

The wire rope model has been implemented in Abaqus/Standard<sup>®</sup> and is representative of a part of a longer wire rope. We first begin this section by presenting the new contact and friction element. After introducing the basic principles, we show the comparison of the results on a simple benchmark of a simplified rope, to analytic solutions and to results obtained with a large-sliding algorithm employing surface elements to track the position of the wire surfaces. The second part of this section illustrates the boundary conditions of the detailed wire rope model, from which periodicity is imposed to represent the wire rope continuity.

### 2.1 A New Contact and Friction Element for Wire Rope

Resuming the beam-to-beam strategy of [14] with linear beam elements, we use here a different contact and friction algorithm with a higher computational efficiency, assuming small sliding between the wires. Only the basic principles of the model are presented here. The reader could find more details on this model in [23, 24].

The user-element is a two-node contact element for non parallel beams. Note that we do not consider the lateral contact between wires of a same layer. Its connectivity is defined initially and the contact pairing is fixed along the analysis. Considering a wire rope, the initial contact positions can be determined by trivial geometrical operations.

Let us consider at the initial state, the contact among two nodes at positions  $\mathbf{X}_1$  and  $\mathbf{X}_2$  located on two wires in adjacent layers (Fig. 1). The wires have circular cross sections of radius  $r_1$  and  $r_2$  respectively, and we neglect the Poisson effect, which seems reasonable for standard steel wires. The initial beam tangent vectors are denoted  $\mathbf{T}_1$  and  $\mathbf{T}_2$ . As usual in contact algorithms among non parallel beams [15, 16, 22], the contact normal is defined as the normalized vectorial product of the beam tangents.

In the deformed configuration, the position vectors of the nodes are respectively  $\mathbf{x}_1$  and  $\mathbf{x}_2$ . In general they are no more coincident with the points on the beam axes

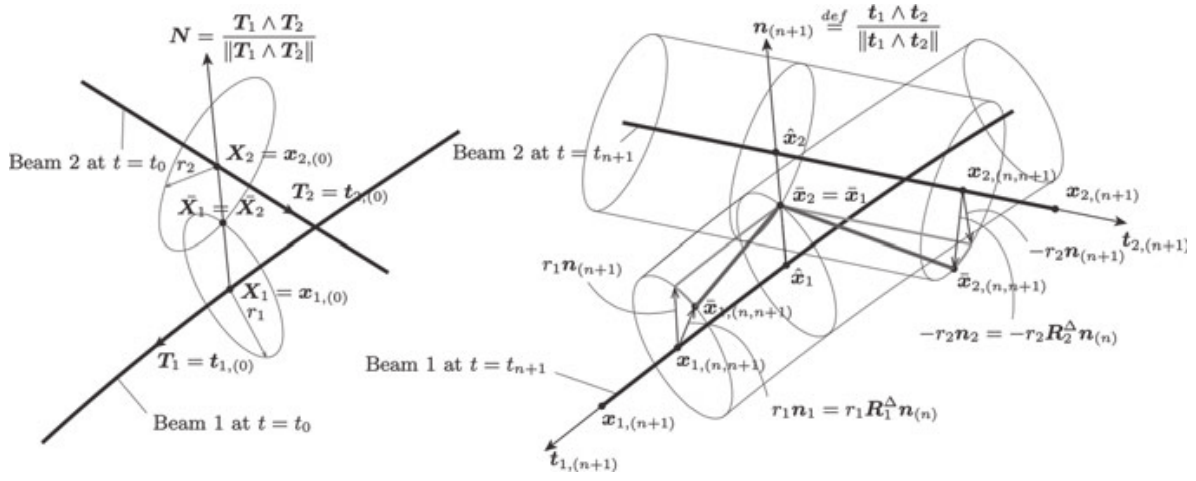


**Fig. 1** Beam-to-beam contact kinematics: initial and deformed configurations

that minimize the distance among the beams, i.e. the points  $\hat{\mathbf{x}}_1$  and  $\hat{\mathbf{x}}_2$  in Fig. 1. If the relative sliding is small, we can reasonably state

$$\hat{\mathbf{x}}_1 \approx \mathbf{x}_1 + \xi^1 \mathbf{t}_1(\mathbf{x}_1) \quad \hat{\mathbf{x}}_2 \approx \mathbf{x}_2 - \xi^2 \mathbf{t}_2(\mathbf{x}_2) \quad (1)$$

which basically consists in assuming that the beams are straight in proximity of the initial contact position. Accordingly, for the normal contact vector we have

$$\mathbf{n} = \frac{\mathbf{t}_1(\hat{\mathbf{x}}_1) \wedge \mathbf{t}_2(\hat{\mathbf{x}}_2)}{\|\mathbf{t}_1(\hat{\mathbf{x}}_1) \wedge \mathbf{t}_2(\hat{\mathbf{x}}_2)\|} \approx \frac{\mathbf{t}_1(\mathbf{x}_1) \wedge \mathbf{t}_2(\mathbf{x}_2)}{\|\mathbf{t}_1(\mathbf{x}_1) \wedge \mathbf{t}_2(\mathbf{x}_2)\|} \quad (2)$$

Finally the normal gap can be defined as

$$g_N = (\mathbf{x}_2 - \mathbf{x}_1) \cdot \mathbf{n} - (r_1 + r_2) \quad (3)$$

A particular difference with [25] concerns the definition of the tangential gap increment  $\mathbf{g}_T^\Delta$ , which is the relative displacement experienced by the material points  $\bar{\mathbf{x}}_1$  and  $\bar{\mathbf{x}}_2$  that were in contact in configuration at  $t_n$ , projected on the new tangential plane in configuration  $t_{n+1}$ .

Firstly,  $\bar{\mathbf{x}}_1$  and  $\bar{\mathbf{x}}_2$  are mapped in the new configuration at  $t_{n+1}$  (Fig. 1). These new positions are denoted respectively  $\bar{\mathbf{x}}_{1,(n,n+1)}$  and  $\bar{\mathbf{x}}_{2,(n,n+1)}$ , where first index  $n$  refers to the fact that they were the material points in contact at configuration  $n$  and second index  $n + 1$  refers to the configuration where the material points are mapped. The new material points in contact are simply denoted by  $\bar{\mathbf{x}}_{1,(n+1)}$  and  $\bar{\mathbf{x}}_{2,(n+1)}$ .

For each beam, on time increment  $\Delta t_{n+1} = t_{n+1} - t_n$ , the distance between the previous material point in contact in configuration  $n$  and the current material point in contact at configuration  $n + 1$  can be defined for each beam as

$$\begin{cases} \mathbf{d}_1^\Delta = \bar{\mathbf{x}}_{1,(n,n+1)} - \bar{\mathbf{x}}_{1,(n+1)} \\ \mathbf{d}_2^\Delta = \bar{\mathbf{x}}_{2,(n,n+1)} - \bar{\mathbf{x}}_{2,(n+1)} \end{cases} \quad (4)$$

The normal direction changes in the new configuration and is defined by:

$$\mathbf{n}_{(n+1)} \stackrel{def}{=} \frac{\mathbf{t}_{1,(n+1)} \wedge \mathbf{t}_{2,(n+1)}}{\|\mathbf{t}_{1,(n+1)} \wedge \mathbf{t}_{2,(n+1)}\|}$$

where  $\mathbf{t}_{i,(n+1)} = \mathbf{t}_i(\mathbf{x}_{i,(n+1)})$  denotes the current director of beam  $i$  at the node  $\mathbf{x}_{i,(n+1)}$ .

The increment of tangential gap  $\mathbf{g}_T^\Delta$  is defined as the projection of the difference between  $\mathbf{d}_2^\Delta$  and  $\mathbf{d}_1^\Delta$  in the current tangent contact plane at configuration  $n + 1$ . To alleviate the notation, the subscript  $(n + 1)$  to indicate a quantity referred to the current time increment will be discarded from now on. One has:

$$\mathbf{g}_T^\Delta = (\mathbf{I}_d - \mathbf{n} \otimes \mathbf{n})(\mathbf{d}_2^\Delta - \mathbf{d}_1^\Delta) \quad (5)$$

with

$$\begin{aligned} \mathbf{d}_1^\Delta &= \mathbf{x}_1 + \xi_{(n)}^1 \mathbf{t}_1 + r_1 \mathbf{n}_1 - (\mathbf{x}_1 + \xi^1 \mathbf{t}_1 + r_1 \mathbf{n}) \\ &= -(\xi^1 - \xi_{(n)}^1) \mathbf{t}_1 + r_1 (\mathbf{n}_1 - \mathbf{n}) \\ \mathbf{d}_2^\Delta &= \mathbf{x}_2 - \xi_{(n)}^2 \mathbf{t}_2 - r_2 \mathbf{n}_2 - (\mathbf{x}_2 - \xi^2 \mathbf{t}_1 - r_2 \mathbf{n}) \\ &= (\xi^2 - \xi_{(n)}^2) \mathbf{t}_2 - r_2 (\mathbf{n}_2 - \mathbf{n}) \end{aligned} \quad (6)$$

$$\mathbf{n}_1 = \mathbf{R}_1^\Delta \mathbf{n}_{(n)}; \quad \mathbf{R}_1^\Delta = \mathbf{R}(\Phi_1^\Delta) \quad (7)$$

$$\mathbf{n}_2 = \mathbf{R}_2^\Delta \mathbf{n}_{(n)}; \quad \mathbf{R}_2^\Delta = \mathbf{R}(\Phi_2^\Delta) \quad (8)$$

and in which  $\Phi_i^\Delta$  is the rotation in the current increment of beam  $i$ . Therefore one gets

$$\begin{aligned} \mathbf{g}_T^\Delta &= (\mathbf{I}_d - \mathbf{n} \otimes \mathbf{n})[(\xi^i - \xi_{(n)}^i) \mathbf{t}_i - r_i \mathbf{n}_i] \\ &= (\xi^i - \xi_{(n)}^i) \mathbf{t}_i - (\mathbf{I}_d - \mathbf{n} \otimes \mathbf{n}) r_i \mathbf{n}_i \end{aligned} \quad (9)$$

This definition of  $\mathbf{g}_T^\Delta$  is equivalent of quantifying the amount of relative sliding by approximating the actual movement histories by straight lines projected on the contact tangent plane at configuration  $n + 1$ . It is clear that the more the time step decreases, the better the approximation of the theoretical path of the contact material point on each beam is. It can be noted that with this definition of  $\mathbf{g}_T^\Delta$  also relative movements generated by rolling are taken into account.

First terms  $(\xi^i - \xi_{(n)}^i) \mathbf{t}_i$  reflect the relative sliding in the beam axes direction and the term  $(\mathbf{I}_d - \mathbf{n} \otimes \mathbf{n})(r_1 \mathbf{n}_1 + r_2 \mathbf{n}_2)$  is associated with sliding along the circumferential directions of each beam. This second term is not considered when the contact problem between beams is treated as contact between curves, as occurs in [16]. In other words, the sliding between curves can be described by the evolution of the parameters  $\xi^i$ , while the characterization of the sliding between the beam surfaces, being two-dimensional, requires two components. This has been done for instance in [21], where the beam surfaces are described by couples of convective coordinates.

The tangential gap function at configuration  $n + 1$  can now be defined by:

$$\mathbf{g}_T = \mathbf{g}_T^\Delta + \mathbf{g}_{T,(n,n+1)} \quad (10)$$

with  $\mathbf{g}_{T,(n,n+1)}$  the elastic part of the tangential sliding at increment  $n$  mapped in the current configuration  $n + 1$ . Namely, provided that the angle between beams (i.e. scalar product  $\mathbf{t}_1 \cdot \mathbf{t}_2$ ) does not change to much during a time-step, this mapping is performed as follows:

$$\mathbf{g}_{T,(n)} = \xi_{(n)}^e \mathbf{t}_{i,(n)} \longrightarrow \mathbf{g}_{T,(n,n+1)} = \xi_{(n)}^e \mathbf{t}_i \quad (11)$$

Friction satisfies a classical Coulomb's law with a return mapping procedure to compute the increment when the sliding criterion is reached.

The contact forces are obtained by applying a penalty method. The penalty coefficients are chosen in order to limit the penetration of the contacting bodies, which specifically in wire rope modeling can have an important influence on the quantities estimated. A high penetration would in fact cause an artificial compression of the wires, and consequently also lower normal contact forces. Similarly, the discontinuity of the Coulomb friction law is regularized by an elastic slip. In choosing the regularization value, one should also take care that too high values could lead to bad conditioning of the tangent matrix to be inverted in the linearized balance of momentum equation. Nevertheless, the elastic slip value can significantly influence the results when small variations of curvature of the rope axis are involved.

The complete expressions of the variational formulation of this model and of its linearization are detailed in [23].

## 2.2 *Comparison to Analytical and Surface to Surface Solutions*

We now propose to check the approximation of the small sliding assumption in the contact and friction model by applying it to a simplified rope model. The model is composed of a central wire, a layer of six helical wires and a single helical wire wrapped around (Fig. 2). All the wires are identical, with radius  $r = 2.15$  mm and linear elastic material properties  $E = 210$  GPa and  $\nu = 0.3$ . The friction coefficient is set to 0.5. The lay angle is  $12^\circ$  for both layers, with opposite laying orientations. The length of the model corresponds to two times the lay length of external helix, i.e. 254.2 mm.

The end nodes of the helical wires are linked via a kinematic coupling to the end nodes of the central wire. In particular, a plane end section kinematics is imposed, but the displacement and the rotation respectively in and around the radial direction are left free. The central wire kinematics is fully controlled in such a way to impose a constant axial strain  $\varepsilon = 1.e - 3$  and constant curvature  $\kappa$  with no change of the

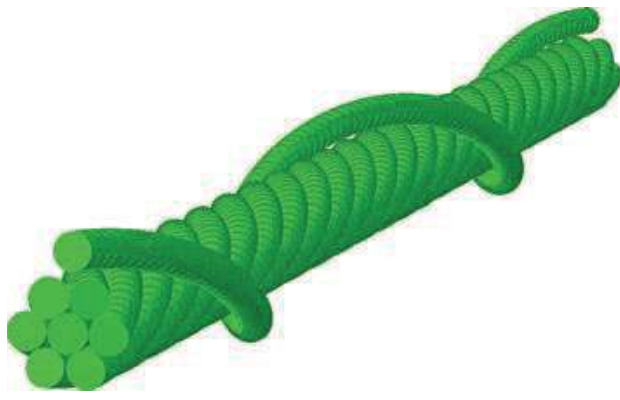


**Fig. 2** Benchmark test used to validate the wire rope model

bending axis. For symmetry reason (see e.g. [11]), the sliding of a wire relative to the underneath layer should be zero at the outer and inner-arc. One should note that the external helix ends are located at the outer-arc, therefore the boundary conditions are correct for this helix kinematic, but could introduce a small error for the kinematics of the underneath layer. This problem will be addressed with a periodic condition in the next section.

The axial force in the external helix obtained with the new beam-to-beam frictional contact element are compared to analytical solutions assuming negligible radial displacement, sliding with respect to the underneath layer along the helix, and a complete stick or a complete slip state [11]. The amplitude of displacement of the same helix are compared to that obtained with a model representing the contact and friction between surface elements meshing the wire surface. These surface elements are rigidly linked to the node in the same wire section, on the wire beam.

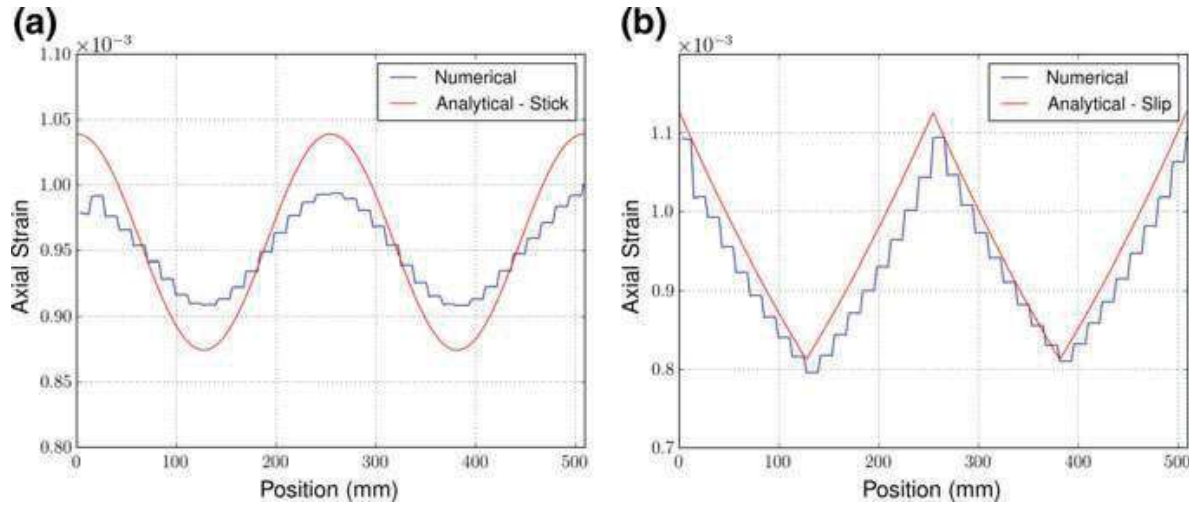
The regularization of the contact law and the Coulomb friction law are achieved by a penalty coefficient  $\varepsilon_N$  and an elastic slip  $\gamma_e$ , respectively. For the comparison to the numerical surface-to-surface,  $\gamma_e = 1.e - 2$  mm and  $\varepsilon_N = 2.e3$  N/mm for the beam-to-beam and  $\varepsilon_N = 1.e4$  N/mm for the surface-to-surface. For the comparison with the analytical solution, we select a higher contact stiffness both in normal and in tangential direction, using  $\varepsilon_N = 2.e5$  N/mm and  $\gamma_e = 1.e - 4$  mm.

Figure 4 reports the axial force in the external helical wire, for a stick and slip states [(a) and (b), respectively]. The difference in amplitude for the stick state can be explained by the penalty regularization of contact, and the under-constrained nodes which are not in contact. This localized property of contact in trellis contact is a marked difference with the line contact assumption of the analytical model, as illustrated in Fig. 3.

Figure 5 shows the Euclidean norm of the sliding of the external helix for the new beam-to-beam and the surface-to-surface algorithms. This sliding is determined with respect to a reference cylinder, whose axis is the one of the rope, its radius is the one of the external helix and whose cross sections follow the Euler-Bernoulli beam kinematics. The results compare successfully for the slip state. Small differences are however visible in the stick state. They could be explained by considering that the beam-to-beam algorithm neglects a rigidity of the surface-to-surface friction with respect to a relative rotation of the beams around the contact normal. This is linked



**Fig. 3** Contact areas displayed for the benchmark 2 in the surface-to-surface model



**Fig. 4** Axial force distribution in the helix of the second layer for (a)  $\kappa = 1.e - 5 \text{ mm}^{-1}$  and (b)  $\kappa = 1.e - 3 \text{ mm}^{-1}$

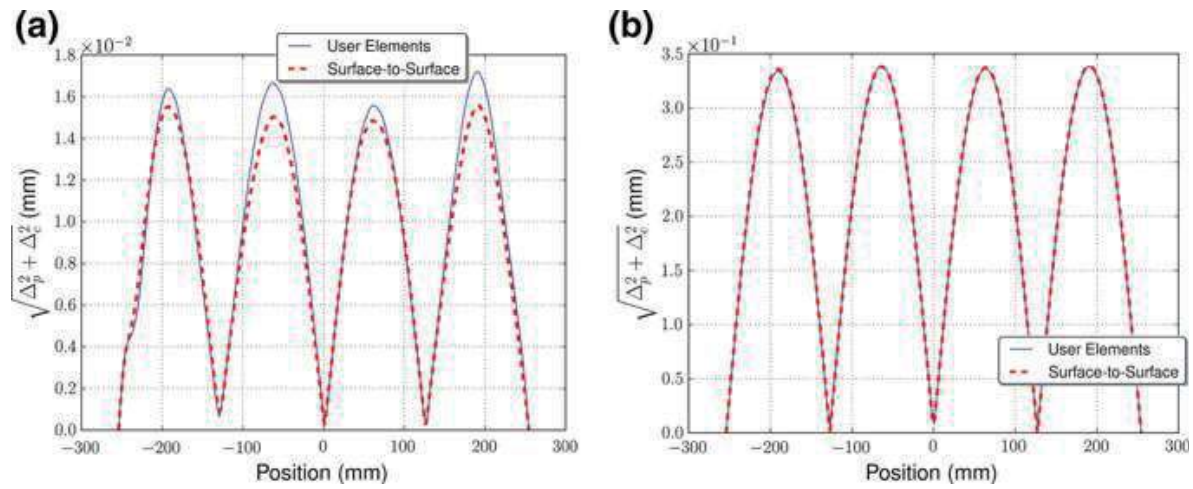


**Fig. 5** Total slip comparison: (a)  $\kappa = 5.e - 5 \text{ mm}^{-1}$  (b)  $\kappa = 1.e - 3 \text{ mm}^{-1}$

to the pointwise contact approximation, while in the surface-to-surface model the contact is spread on finite surfaces (Fig. 3).

In view of these results, we can see that the new beam-to-beam element produces an acceptable approximation of the large sliding surface-to-surface contact and friction between the wires of a spiral strand wire rope. Since it does not update the contact pairing, and also because the contact normal varies smoothly (it depends only on the rotation of the wire sections), it facilitates the Newton convergence, and leads to a gain in CPU time. Indeed, when comparing for this simplified case to a large sliding beam-to-beam algorithm of Abaqus/Standard<sup>®</sup>, the CPU time reduction gives a ratio of about 20.

The reader could find a more detailed comparison of the results obtained on different test cases with this new contact and friction elements to the results obtained with large sliding beam-to-beam algorithms available in legacy software or in the literature in [23].

### 2.3 *Boundary Conditions*

In order to simulate the continuity of the rope, a strategy to impose properly the boundary conditions has been developed. The kinematics of the central wire is fully controlled, since constant axial strain and curvature are imposed to respect the output of the FOWT model. The bending axis does not change along the analysis. It is assumed that this simplifying hypothesis overestimates load variation on some wires and is thus conservative for the fatigue.

The boundary conditions are imposed via a Multi-Point Constraint (MPC) user-subroutine. An important result coming from the analytical models is here exploited. When a wire rope is bent, relative displacements among the wires of adjacent layers may occur according to the curvature, to the applied tension and to the friction coefficient between the contacting wires [11]. Consequently, when sliding occurs, initial plane cross sections are in general not plane anymore in the bent configuration.

When bent, a position along the wire can be parameterized by a circumferential angle  $\theta$  from  $\pi/2$  at the outer-arc to  $-\pi/2$  at the inner arc (Fig. 6). The analytical axial force distribution in a helical wire of a bent wire rope geometrically depends on  $\sin(\theta)$  in the stick state (Fig. 4a). Hence, positions at  $\theta = \pm\frac{\pi}{2}$  are symmetry points (with no relative displacement) which rotate with the rope cross section.

Let us consider a wire rope portion whose axis has constant axial deformation and curvature. To facilitate the explanation, consider first the external layer for which the lay length (i.e. the initial periodic length) defines the model length. A wire of this layer, called *reference wire*, is set to have its extremities at outer-arc locations  $\theta = \pm\frac{\pi}{2}$ , for example  $Q$  in Fig. 7. The nodes at these extremities are linked to the corresponding nodes of the central wire in such a way that they stay on the same wire rope cross section in the bent configuration, meaning that we impose zero relative displacement with respect to the central wire, and they keep the same position  $\theta$  on this cross section (we do not consider wire rope torsion). Because they are at outer-arc

**Fig. 6** The angle  $\theta$  identifies the position of a wire in the cross section with respect to the bending axis

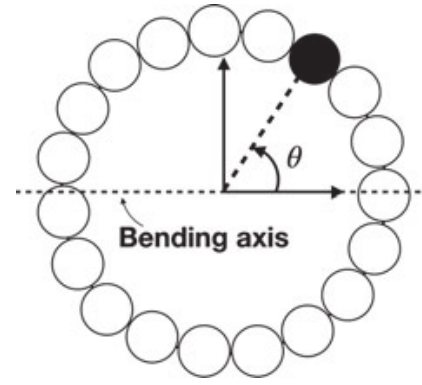
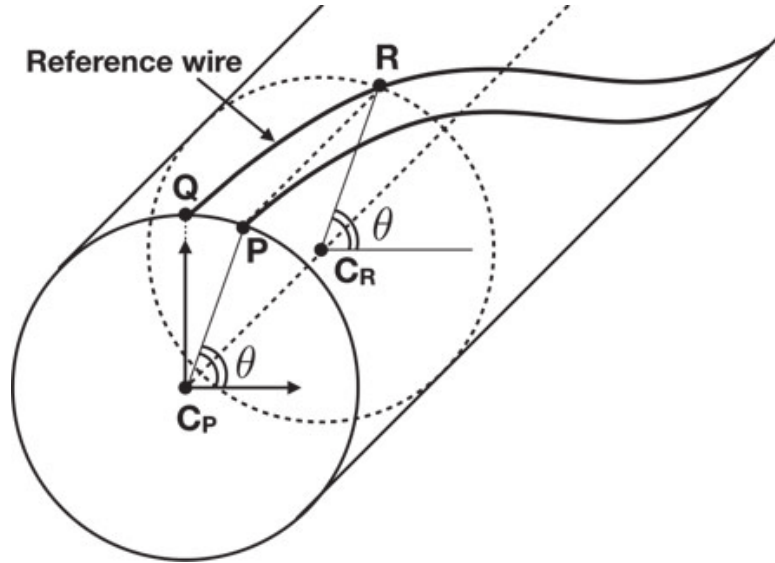


**Fig. 7** Points involved in a MPC



locations, this kinematic link is not conflictual with the natural wire kinematics during bending. Now consider another wire of the same external layer which extremity  $P$  is not at the outer-arc. To model the rope continuity, the kinematic of  $P$  is defined by the Abaqus/Standard Multi Point Constraint (MPC) as follows. The points involved in each MPC are four and are represented in Fig. 7:

- the point  $P$  is the one to which the constraint is imposed (i.e. the slave node), since  $\theta_P \neq \pm \frac{\pi}{2}$ ;
- the point  $C_P$  is the node of the central wire in the cross section containing the points  $Q$  and  $P$ ;
- the point  $R$  is the node on the reference wire for which  $\theta_R = \theta_P$
- the point  $C_R$  is the node on the central wire in the cross section containing  $R$ .

Note that point  $Q$  (Fig. 7) is kinematically linked to  $C_P$  to stay in the same cross section and at the same angle  $\theta$ . In general, points  $R$  and  $C_R$  are arbitrary with respect to the mesh nodes. The FEM interpolation however enables to relate the degrees of freedom at these locations to that of the elements they belong.

The constraint equation for displacement imposes that the relative sliding of point  $P$  with respect to  $C_P$  is the same that for point  $R$  with respect to  $C_R$ . The relative sliding of nodes  $P$  and  $R$  are set after rotating back the cross sections with respect to the rotations at points  $C_P$  and  $C_R$ , respectively.

$$\mathbf{R}_{C_P}^T (\mathbf{x}_P - \mathbf{x}_{C_P}) = \mathbf{R}_{C_R}^T (\mathbf{x}_R - \mathbf{x}_{C_R}) \quad (12)$$

where  $\mathbf{R}$  indicates the rotation matrix and  $\mathbf{x}$  the position vector.

For the rotation vectors we simply impose

$$\Phi_P = \Phi_{C_P} \quad (13)$$

See [23] for the detailed linearization. Now consider the case of an internal layer for which only one wire end can be set at an outer-arc location. The other extremity kinematics follows the same relationship that point  $P$  here above, meaning its master point is on the same wire. In [25], if any point of a wire inside the model was at the outer arc (note that for the wire rope considered in the next section, the model length is greater than the lay length of the internal layers), we linked this point to the central wire, as it is done for point  $Q$  here above. We noted that this introduced some numerical artifacts, for reasons to be explained, and thus decided to constrain this point only with contact and friction conditions.

From a study documented in [25] we have noted problems when considering the full linearization terms which are avoided when omitting some terms related to points  $C_P$  and  $C_R$  displacements. Keeping in mind this problem should be solved later, we consider the partial linearization in the following, which obviously degrades the Newton convergence. This strategy however enables to recover a periodic distribution simulating the rope continuity, as indicated by the axial strain in Fig. 8.

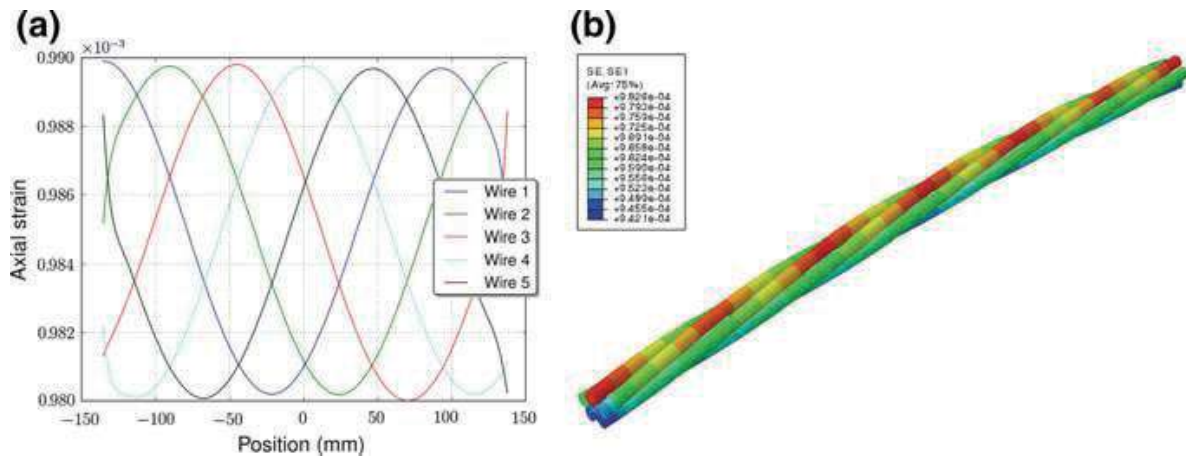


**Fig. 8** (a) Axial strain distribution along the wires and (b) 3D view

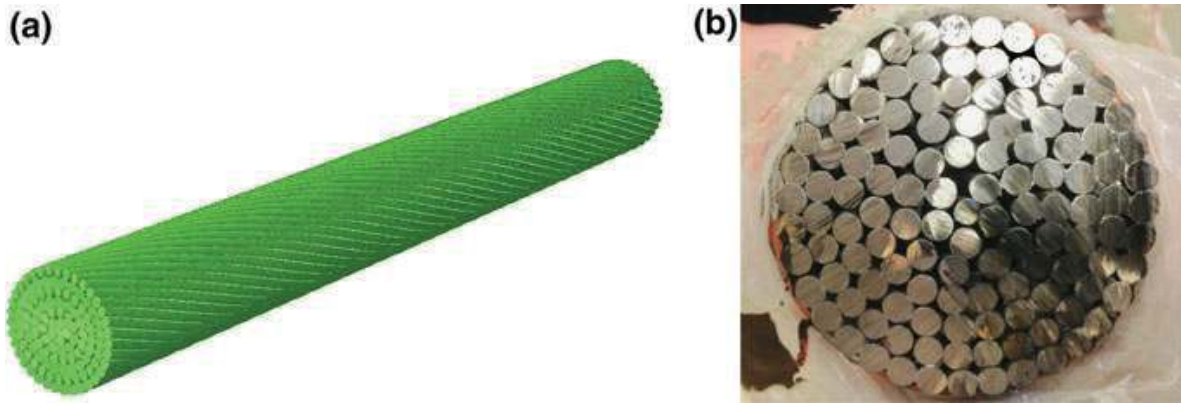


**Fig. 9** (a) Numerical model of the wire rope in Abaqus® and (b) cross section of the chosen wire rope profile

## 2.4 Wire Rope Properties

The wire rope profile has been inspired from a sample provided by Baudin Chateaufneuf company which was designed for a stay-cable bridge. Note that its properties may differ from that of an offshore mooring wire rope which service conditions require specific care concerning the reduction of the tension-torsion coupling. The bending and tensile stiffness of this cable are satisfying the Ultimate Limit State [5] of the case study described in the next section. It is a six-layer steel wire rope (Fig. 9) of 60.4 mm diameter. The layers have alternate lay angle directions and are composed of 5, 11, 17, 23, 29 and 35 wires from the inner to the outer, respectively. The model length is set to the longest pitch which is that of the external layer, i.e. about 580 mm. We have five wires in line contact with the central wire and 5964 trellis contacts. For the steel, we assume a linear elastic behavior, with  $E = 210$  GPa and  $\nu = 0.3$ . The friction coefficient has been set to 0.12, which is the value used in [26] for this type of steel wire ropes after the application of grease.

## 3 Application to a FOWT Model

### 3.1 Global Hydrodynamic FOWT Model

The global model of the FOWT allows to obtain the mechanical states of the whole mooring lines for each sea state to which the structure may be subjected during the structural lifespan. It is implemented in the dedicated hydrodynamic software Deeplines™.

We consider a generic case study of a cylinder-like shape floater, equipped with a redundant mooring system of six catenary mooring lines (Fig. 10) and supporting a downsized version of the NREL 5 MW wind turbine [27] to a 3.6 MW wind turbine. The sea depth is uniform and equal to 100 m. The mooring lines are catenary-shaped

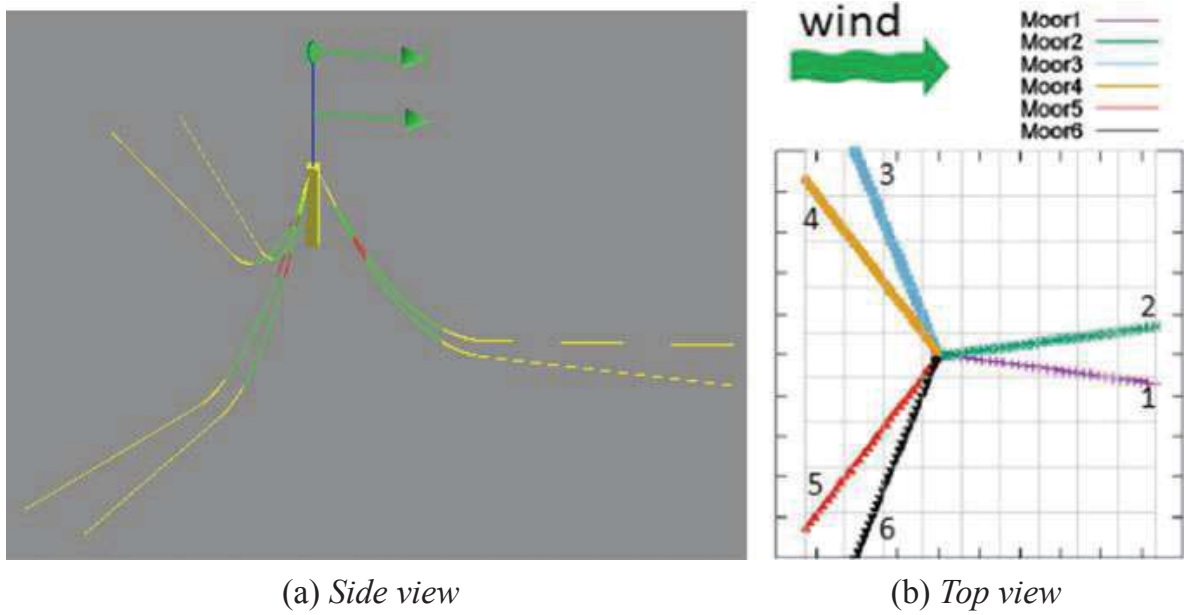


**Fig. 10** (a) Global scale model representation in Deeplines<sup>TM</sup>; (b) top view of the global model, representing the mooring line numbering and their position with respect to the wind direction (which is collinear to the waves)

**Table 1** Mooring lines discretization.  $N_{ele}$  and  $L_{ele}$  denote respectively the number of element and the element length

Parts	$N_{ele}$	$L_{ele}$ (m)
Chain-1	4	7.5
Wire rope-1	2	10.0
Wire rope-2	20	2.0
Wire rope-3	8	12.5
Chain-2	30	5.33
Chain-3	20	11.1

and attached to the floater in three pairs. Their projections on a horizontal plane are equally spaced from one another. Each line has a total length of 572 m (Table 1).

The FOWT is subjected to the action of the environment, i.e. waves and wind. Sea waves are modeled as the superposition of harmonic components, defined by a JONSWAP spectrum [28, 29], fitting the observed Power Spectral Density. The direction of propagation is considered parallel to the wind and does not change along the analysis. We consider the long-term statistical distribution given by metocean data gathered from an offshore site in the west of France, from which the Wave Scatter Diagram (WSD) is reported in Fig. 11. Each block of the WSD represents a sea state of three hours, assumed stationary, defined by two parameters of the JONSWAP spectrum, with its percentage of occurrence. These two parameters are the significant wave height ( $H_s$ ), which is related to the integral of the spectrum, and the period of the peak of the spectrum ( $T_p$ ). A third parameter defining the spreading of the JONSWAP spectrum, usually denoted  $\gamma$ , is fixed to 1.3.

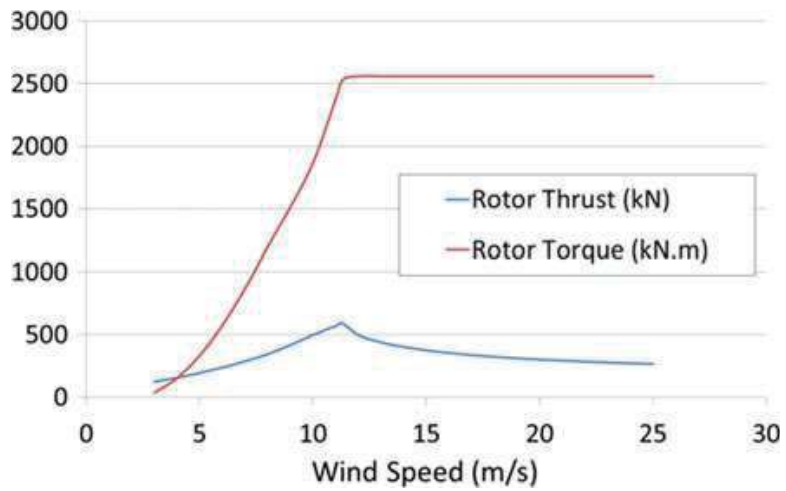
Percentage of occurrence of height of swell (m) in rows versus peak period of swell (s) in columns

lower	upper	2	3	4	5	6	7	8	9	10	11	12	13	14	15	16	17	18	19	20	21	22	23	24	25	total
0	0,5	0	0,005	0,003	0,037	0,166	0,318	0,555	0,658	0,634	0,51	0,446	0,303	0,22	0	0,182	0,149	0	0,075	0	0,036	0	0,019	0	0	4,316
0,5	1	0	0	0	0,072	0,308	0,625	1,117	1,302	1,117	0,801	0,618	0,346	0,2	0	0,099	0,033	0	0,007	0	0	0	0	0	0	6,845
1	1,5	0	0	0	0,003	0,039	0,282	0,542	1,148	1,62	1,6	1,191	0,869	0,45	0,193	0	0,104	0,043	0	0,009	0	0,002	0	0	0	8,097
1,5	2	0	0	0	0,002	0,06	0,252	0,671	1,03	1,528	1,338	1,052	0,537	0,168	0	0,111	0,026	0	0,01	0	0,002	0	0	0	0	8,802
2	2,5	0	0	0	0	0,003	0,072	0,277	0,527	0,963	1,354	1,28	0,633	0,216	0	0,064	0,012	0	0,007	0	0	0	0	0	0	5,438
2,5	3	0	0	0	0	0	0,012	0,062	0,202	0,477	0,883	1,068	0,664	0,187	0	0,074	0,019	0	0	0	0	0	0	0	0	3,646
3	3,5	0	0	0	0	0	0,014	0,072	0,27	0,607	0,963	0,601	0,144	0	0,056	0,01	0	0,002	0	0	0	0	0	0	0	2,74
3,5	4	0	0	0	0	0	0	0,015	0,121	0,298	0,671	0,618	0,156	0	0,033	0,01	0	0	0	0	0	0	0	0	0	1,91
4	4,5	0	0	0	0	0	0	0,002	0,026	0,176	0,448	0,423	0,214	0	0,034	0,015	0	0	0	0	0	0	0	0	0	1,338
4,5	5	0	0	0	0	0	0	0	0,012	0,056	0,33	0,347	0,238	0	0,077	0,017	0	0,003	0	0	0	0	0	0	0	1,081
5	5,5	0	0	0	0	0	0	0	0	0,019	0,147	0,291	0,149	0	0,06	0,009	0	0	0	0	0	0	0	0	0	0,674
5,5	6	0	0	0	0	0	0	0	0	0	0,063	0,099	0,115	0	0,058	0,019	0	0,003	0	0	0	0	0	0	0	0,358
6	6,5	0	0	0	0	0	0	0	0	0	0,002	0,01	0,063	0,096	0	0,077	0,015	0	0	0	0	0	0	0	0	0,264
6,5	7	0	0	0	0	0	0	0	0	0	0	0,005	0,015	0,054	0	0,039	0,005	0	0	0	0	0	0	0	0	0,123
7	7,5	0	0	0	0	0	0	0	0	0	0	0,012	0,019	0	0,022	0,009	0	0	0	0	0	0	0	0	0	0,062
7,5	8	0	0	0	0	0	0	0	0	0	0	0,005	0,005	0	0,019	0,003	0	0,002	0	0	0	0	0	0	0	0,034
8	8,5	0	0	0	0	0	0	0	0	0	0	0,003	0,003	0	0,009	0,005	0	0	0	0	0	0	0	0	0	0,021
8,5	9	0	0	0	0	0	0	0	0	0	0	0	0,003	0	0,007	0	0	0	0	0	0	0	0	0	0	0,01
9	9,5	0	0	0	0	0	0	0	0	0	0	0	0	0	0	0	0	0	0	0	0	0	0	0	0	0
total		0	0,005	0,007	0,15	0,84	2,021	3,844	5,429	6,749	7,219	7,972	5,415	2,378	0	1,155	0,399	0	0,117	0	0,039	0	0,019	0	0	43,758

Copyright ARGOSS, November 2012

**Fig. 11** Wave scatter diagram of a particular azimuthal sector. Rows represent bins of the significant wave height  $H_s$  (m). Columns represent bins of the peak period  $T_p$  (s)

**Fig. 12** Thrust and torque on the rotor of the 3.6 MW turbine as function of the wind speed, computed by the software DeeplinesWind<sup>TM</sup>



For the sake of simplicity and to focus on mooring modeling, aero-dynamic influence will be accounted for only by steady wind thrust applied on the tower and torque applied on the nacelle, whose magnitudes depend on the mean wind speed as shown in Fig. 12. This simplification could be supported if assuming a smaller wind than wave influence on the mooring line tension, as suggested for example in [30] for another semi-submersible floater.

Each mooring line is composed of three parts, with chains at the extremities and spiral strand ropes in between.

Wire ropes are modeled by linear beam elements, whose formulation takes into account large rotations [31]. We neglect the tension-torsion coupling, and consider a high torsional stiffness of  $1.e6 \text{ Nm}^2/\text{rad}$ . The modeling of the bending behavior has been determined after preliminary computations, as will be detailed in Sect. 3.2.

One additional mass of 2 tons is distributed in the “Wire rope-2” part (see Table 1) of each mooring line, in order to limit the floater movements and to keep the lines in tension. Chains have no bending stiffness and are therefore modeled by bar elements. The finite element discretization is reported in Table 1.

Contact between mooring lines and seabed is assumed frictionless and it is modeled according to [32]. A penalty regularization is used with a linear contact stiffness of  $1.e6 \text{ N/mm}^2$ .

The floater is considered as a rigid body. Its behavior is represented by Response Amplitude Operators (RAO, i.e. transfer function with respect to wave period and wave elevation) of its displacement and rotation degrees of freedom. The RAO are computed in another software from linear hydrodynamic computations of diffraction and radiation components. The forces and moments acting on the floater are computed by the superposition of the RAO of the different harmonic components of the stochastic realization of the sea state.

The main hydrodynamic loading on the mooring lines are the drag forces, which are represented by the classical Morison's equation. This approach is an approximation justified by the fact that the line diameter is much smaller than the wavelength [33, 34].

### 3.2 Global Model Results

As explained in analytical approaches [9–11], wire rope bending stiffness depends on the applied tension, this dependency being disregarded in the FOWT simulation. To investigate its influence on the computed tension and curvature, we consider a non-linear bending stiffness analytically computed according to the methodology given by [10, 11], for an axial strain of  $5e - 4$  (Fig. 13).

Analyses with an extreme sea state (representative of the Ultimate Limit State condition with JONSWAP parameters  $H_s = 10 \text{ m}$  and  $T_p = 14 \text{ s}$ ) have been conducted by choosing either a constant bending stiffness  $EI = EI_{max}$ , i.e. considering the wires completely adherent on each other, or the nonlinear bending stiffness of Fig. 13. The differences in tension and curvature time series are shown in Fig. 14. The tension values are very similar. One notes an offset for the curvature which is

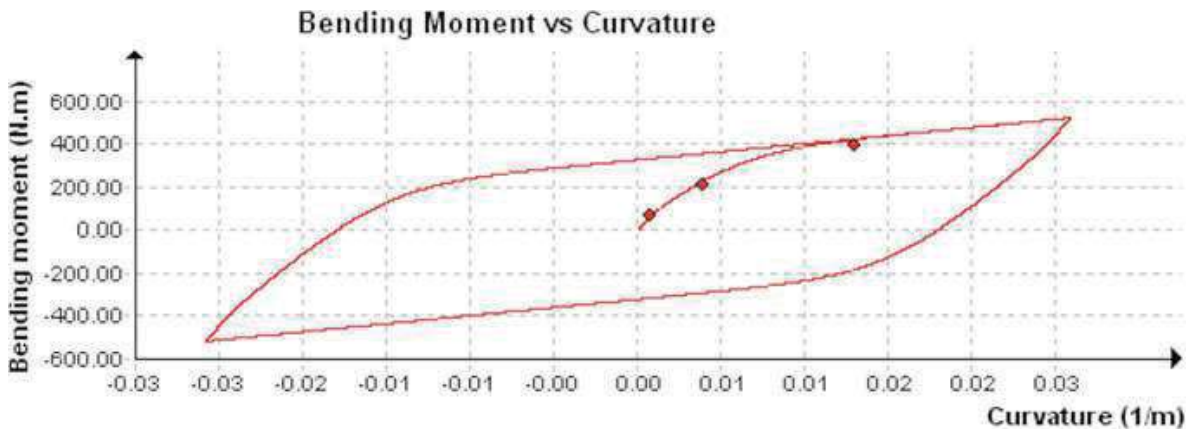


**Fig. 13** Hysteretic bending behavior implemented in Deeplines<sup>TM</sup>, which has been obtained by fitting the bending behavior for  $\varepsilon = 0.5\%$ . Dots show the analytical points

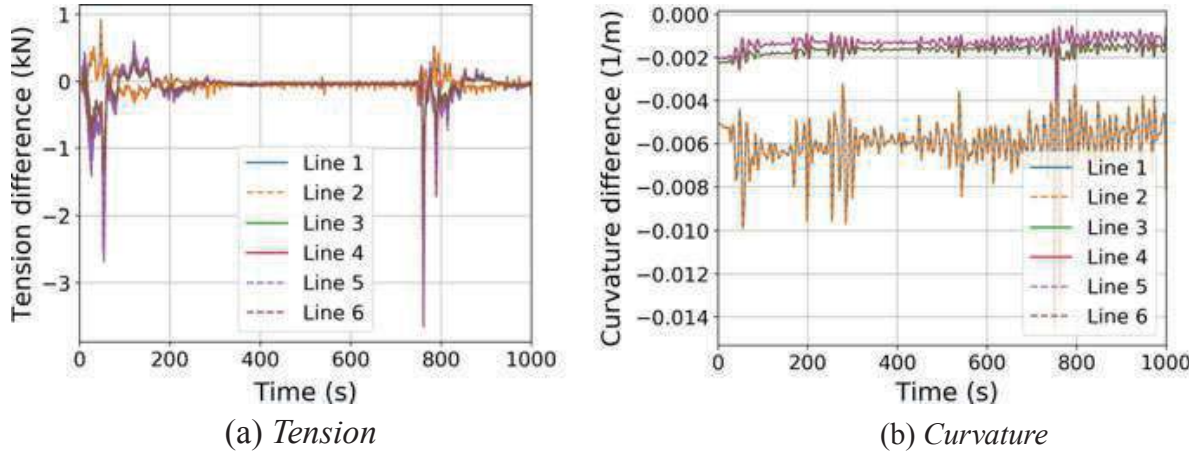


**Fig. 14** Difference of time domain evolution of tension and curvature obtained with  $EI = EI_{max}$  and the nonlinear bending behavior of Fig. 13, for an extreme sea state. These plots are referred to the section most subjected to bending of the lines, which is at  $s = 79$  m

not so important for fatigue by contrast to the amplitude of the variation, for which a difference is observed for very rare high wave amplitudes. Considering this extreme sea state has wave amplitudes noticeably larger than the sea states for the fatigue (Fig. 11), we will assume in the following the global tension and curvature independent on the bending stiffness. In other words, we can adopt a top-down approach uncoupling the global model and the local one.

To simplify the global scale computation, the simulations for all the sea states of the scatter diagram of Fig. 11 have been computed with a constant bending stiffness corresponding to the stick state of wires. Note that we consider simulations of 1000 s only, disregarding the initial 50 s with numerical transient loading. We assume this duration to be long enough to obtain the stationarity of the fatigue damage per unit time. Figures 15 and 16 report the extreme over time of the tension and of the curvature respectively, along the downstream mooring line 1 (Fig. 10b). From them, one can appreciate the range of curvature and tension to which the line is submitted. In particular, we can identify at  $s = 79$  m the most critical zones for what concerns the rope curvature, at the end of the additional mass zones, which will be analyzed with the detailed wire rope model.

### 3.3 Results of the Detailed Wire Rope Model

From Fig. 16, we selected the position at 79 m from the top, along the mooring line 1, to be simulated with the detailed wire rope model. Input tension and curvature have been computed for a severe fatigue sea state with  $H_s = 8.75$  m and  $T_p = 16.5$  s wave parameters (see Fig. 11) and are shown in Fig. 17. The corresponding wave elevation time series is shown in Fig. 18. The initialization of the loading could not consider the previous history of the wire rope, because of the scatter diagram decomposition. To limit the magnitude of the initial interwire contact forces, we chose to apply the

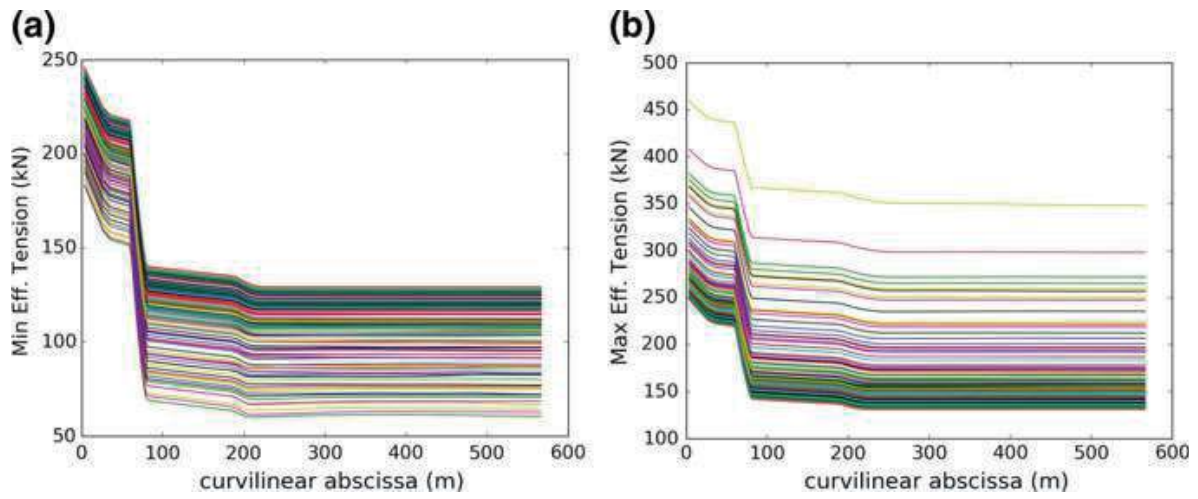


Fig. 15 (a) Min over time and (b) max over time of tension along the mooring line 1

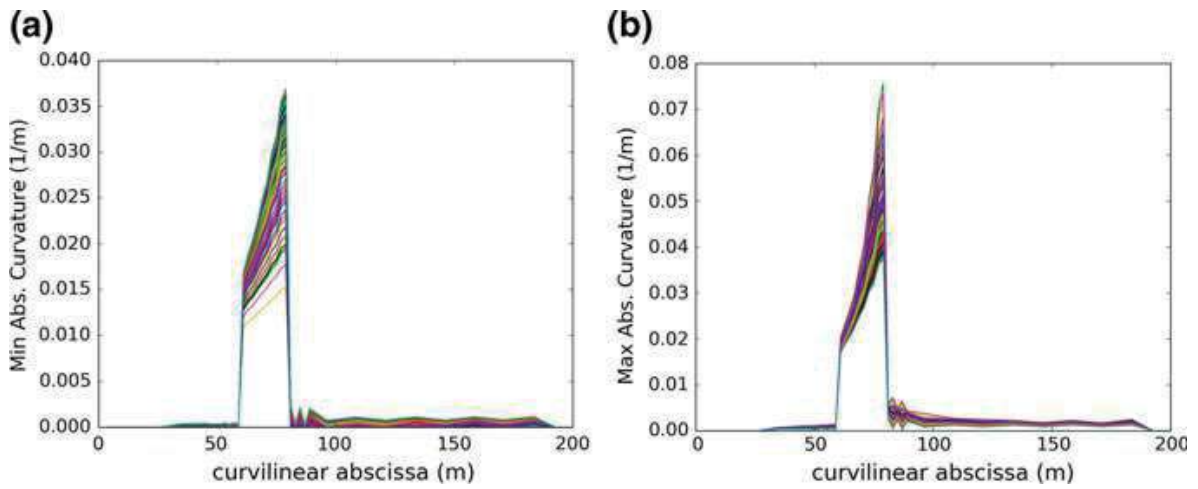


Fig. 16 (a) Min over time and (b) max over time of absolute curvature along the mooring line 1

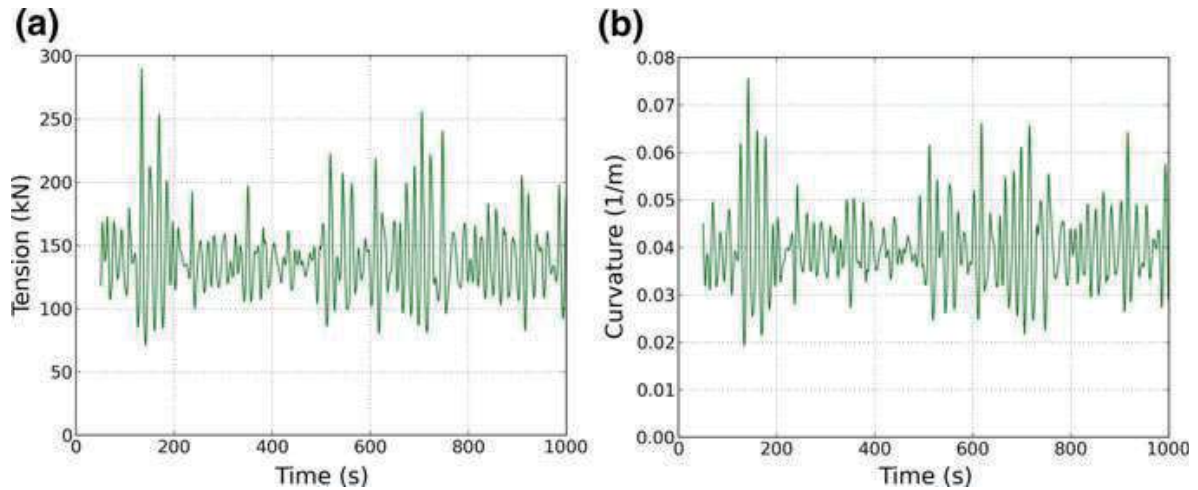
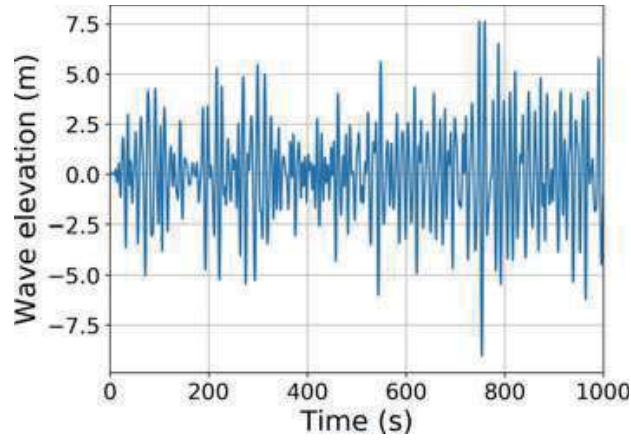
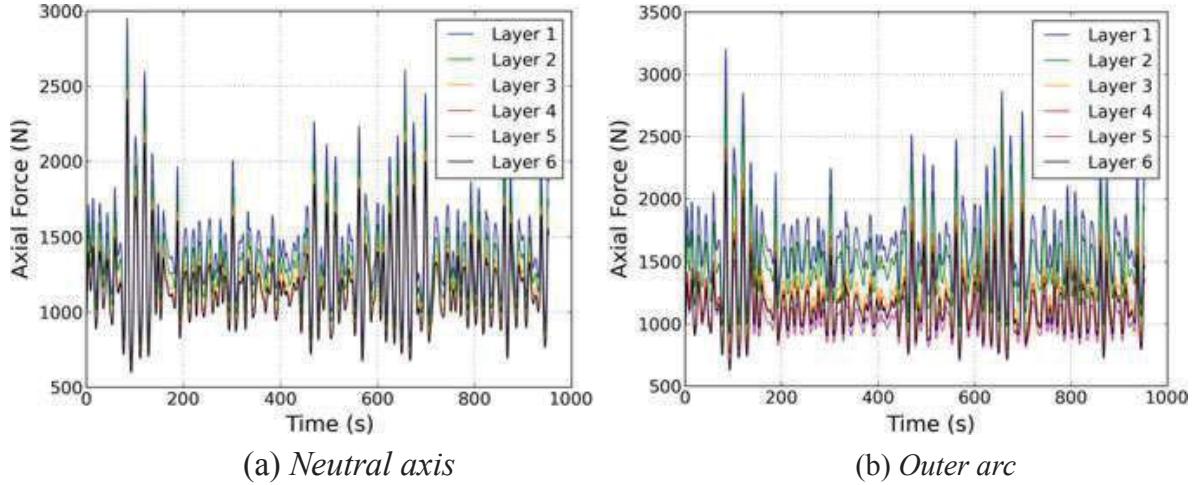


Fig. 17 Time evolution of (a) tension and (b) curvature of the portion of mooring line studied with the detailed wire rope model



**Fig. 18** Wave elevation history considered for the fatigue analysis



**Fig. 19** Time evolution of wire axial force in the proximity of (a) neutral axis and (b) outer arc at each layer

loading in 3 steps: a small tension, a small tension and the initial curvature, and finally the initial tension and curvature.

In Figs. 19, 20 and 21, we report the time evolution of axial force, normal and tangential contact forces at fixed position, in correspondence of the neutral axis and of the outer arc for each layer. For what concern the contact forces, we do not report the values for the first layer, since it is in line contact with the central wire while the others are in contact with the layer underneath at localized positions.

The normal contact forces are higher moving from the external to the internal layers (see Fig. 20). This was expected, since the external layers exert a pressure on the internal ones. At higher normal forces correspond greater tangential forces as well (see Fig. 21).

Because of the lower normal forces, the inter-wire slip is higher for the external layers (Fig. 22). Moreover, the sliding is higher in correspondence of the neutral axis, confirming the experimental evidences [26]. One can see that the wire rope reaches a stabilized state after a time  $t \approx 100$  s, where shift in the sliding is observed at all the interfaces, except the most internal one. By looking at Fig. 18, this time

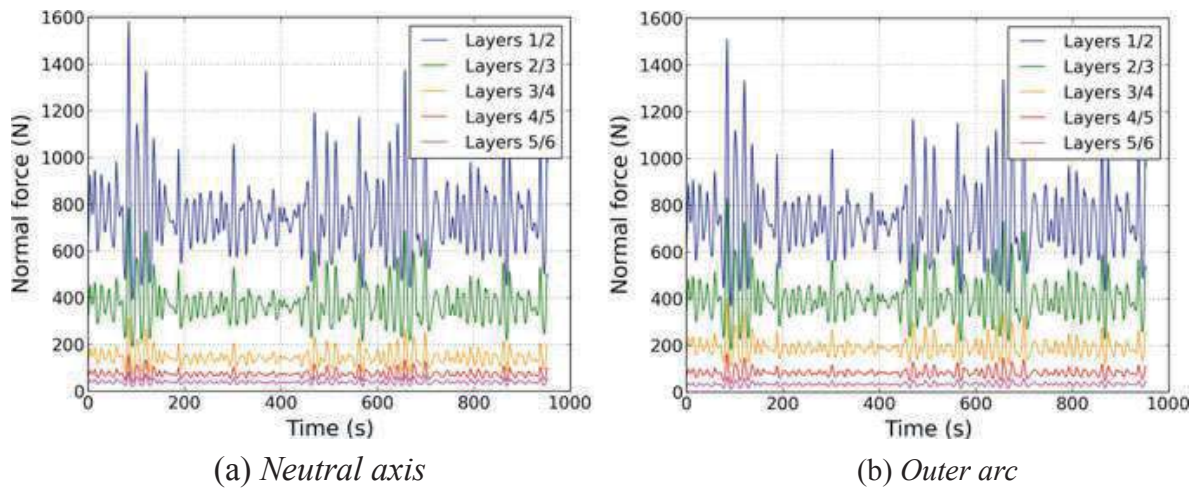


**Fig. 20** Time evolution of normal contact force between two crossing wires in the proximity of (a) neutral axis and (b) outer arc

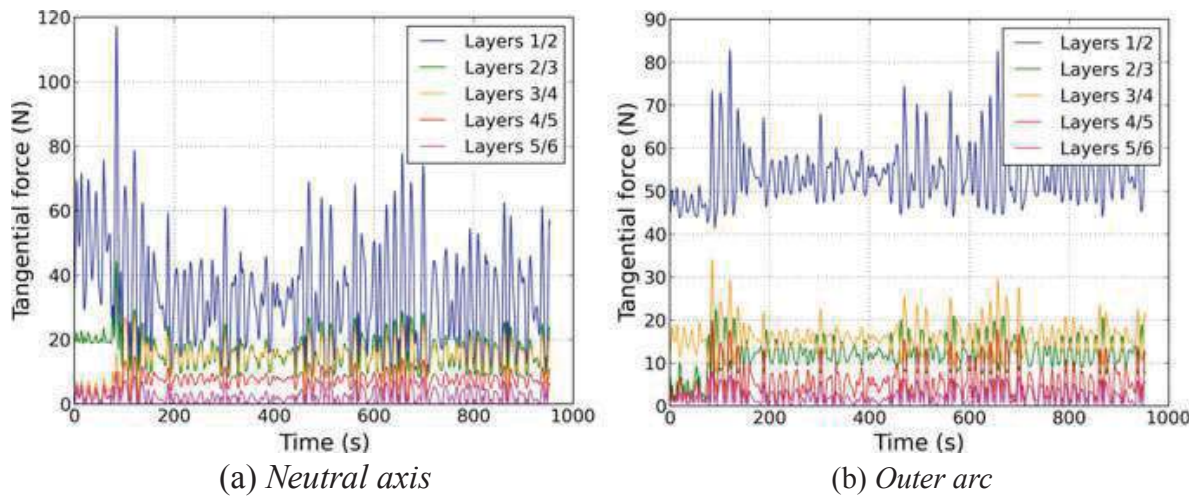


**Fig. 21** Time evolution of tangential contact force between two crossing wires in the proximity of (a) neutral axis and (b) outer arc

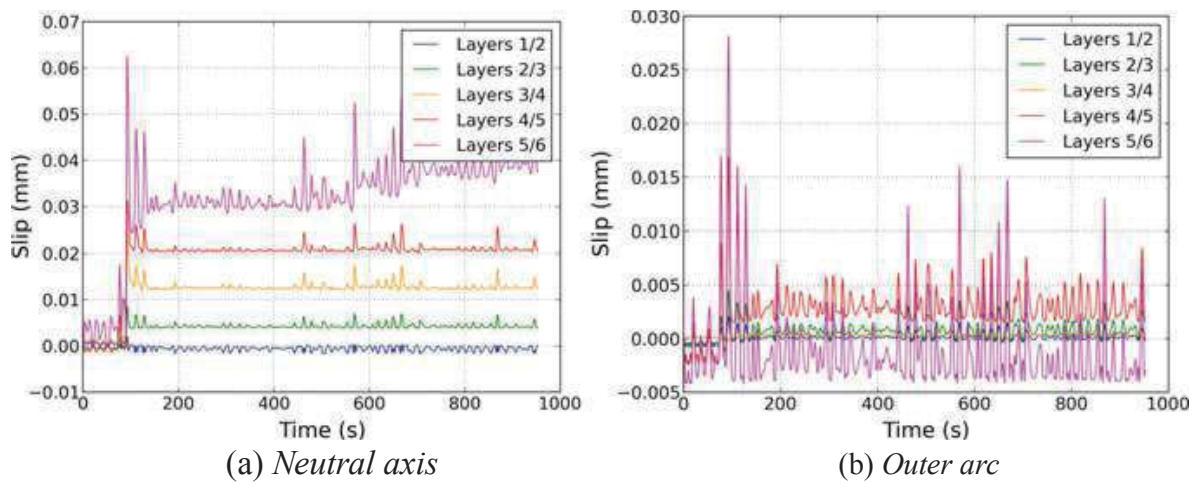


**Fig. 22** Time evolution of inter-wire slip between two crossing wires in the proximity of (a) neutral axis and (b) outer arc

instant does not correspond to a particularly high wave. The inter-wire slip profile could provide an indicator to reveal whether the wire rope response is stabilized or not. Consequently, in this analysis one does not have to rely on the first 100 s. Note that the slip magnitude, for the most external interface, is in the range that activates fretting fatigue (see e.g. [35, 36]). Nevertheless, other analyses have to be performed on less severe sea states to check if the number of fretting cycles can be sufficient to generate fatigue cracks.

## 4 Conclusion

This paper presents a new Finite Element model for simulating the stress at the wire scale of a wire rope in a mooring line of a Floating Offshore Wind Turbine (FOWT). This model is a two-node contact element conceived for the simulation of frictional contact of non-parallel beams. It differs from other models in the literature, as it assumes small sliding of the wires, while updating the contact normal with rope bending. We shown comparison on a simplified case to analytical solutions and a numerical surface-to-surface solution which validate the model approximation. This formulation results in a considerable gain in robustness and CPU times when compared to standard large sliding contact algorithm, which makes this model very interesting for fatigue life estimates, which requires a large number of simulations. This model is implemented as a user subroutine in Abaqus/Standard<sup>®</sup>. A Multi-Point-Constraint (MPC) defines appropriate periodic boundary conditions which are able to simulate the rope continuity.

We present an application for an example of a semi-submersible floater supporting a 3.6 MW wind turbine, equipped with three pairs of catenary mooring lines including six-layer spiral strand wire ropes. The global scale hydrodynamic response of the FOWT is simulated with the software Deeplines<sup>TM</sup>, with steady wind and irregular wave loading. The largest curvature are computed at the bottom of the mooring line portions where additional masses are placed to keep the line in tension. We noted that the nonlinear bending stiffness of the wire rope varying with curvature has a small influence on the resulting tension and curvature, justifying a top-down approach uncoupling the global scale model and the local detailed mechanical model of the wire rope.

Finally the detailed wire rope model has been used to model 1000 s of tension and bending of a severe sea state, showing the potentiality of this model. Further investigations are required in order to validate the obtained results.

Additional work should be necessary to correct the linearization of the periodic boundary conditions. Also, a smaller-scale fretting fatigue analysis should be studied in a future work, including material and corrosion influences, in order to provide the designer a better physically-assessed fatigue constraint.

**Acknowledgements** The authors acknowledge Baudin Chateaufneuf company for having provided the data that inspired the six-layer wire rope model. Principia and FOWT team at IFPEN, in particular Y. Poirette, are thanked for their help in defining the Deeplines™ model. The authors also thank M. Martinez of IFPEN for his help to define the Abaqus/Standard® boundary value problem. This work has been realized during the doctoral thesis of the first author which has been funded by IFP Energies nouvelles.

## References

1. Chaplin, C., & Potts, A. (1991). Wire rope offshore—A critical review of wire rope endurance research affecting offshore applications.
2. Lévesque, F., Goudreau, S., Langlois, S., & Légeron, F. (2015). Experimental study of dynamic bending stiffness of ACSR overhead conductors. *IEEE Transactions on Power Delivery*, *30*(5), 2252–2259.
3. Raoof, M. (1989). Free bending tests on large spiral strands. *Proceedings of the Institution of Civil Engineers*, *87*(4), 605–626.
4. Giglio, M., & Manes, A. (2003). Bending fatigue tests on a metallic wire rope for aircraft rescue hoists. *Engineering Failure Analysis*, *10*(2), 223–235.
5. Det Norske Veritas: Design of floating wind turbine structures. Offshore Standard DNV-OS-J103 (2013).
6. Fontaine, E., Kilner, A., Carra, C., Washington, D., Ma, K., Phadke, A., et al. (2014). Industry survey of past failures, pre-emptive replacements and reported degradations for mooring systems of floating production units. In *Offshore Technology Conference*.
7. Jolicoeur, C., & Cardou, A. (1994). Analytical solution for bending of coaxial orthotropic cylinders. *Journal of Engineering Mechanics*, *120*(12), 2556–2574.
8. Raoof, M., & Hobbs, R. E. (1988). Analysis of multilayered structural strands. *Journal of Engineering Mechanics*, *114*(7), 1166–1182.
9. Costello, G. A. (1997). *Theory of wire rope*. Berlin: Springer Science & Business Media.
10. Hong, K. J., Der Kiureghian, A., & Sackman, J. L. (2005). Bending behavior of helically wrapped cables. *Journal of Engineering Mechanics*, *131*(5), 500–511.
11. Papailiou, K. O. (1995). *Bending of helically twisted cables under variable bending stiffness due to internal friction, tensile force and cable curvature* (Doctoral thesis). ETH, Zurich, Swiss.
12. Judge, R., Yang, Z., Jones, S., & Beattie, G. (2012). Full 3D finite element modelling of spiral strand cables. *Construction and Building Materials*, *35*, 452–459.
13. Zhang, D., & Ostoja-Starzewski, M. (2016). Finite element solutions to the bending stiffness of a single-layered helically wound cable with internal friction. *Journal of Applied Mechanics*, *83*(3), 031003.
14. Lalonde, S., Guilbault, R., & Légeron, F. (2017). Modeling multilayered wire strands, a strategy based on 3D finite element beam-to-beam contacts—Part I: Model formulation and validation. *International Journal of Mechanical Sciences*, *126*, 281–296.
15. Wriggers, P., & Zavarise, G. (1997). On contact between three-dimensional beams undergoing large deflections. *International Journal for Numerical Methods in Biomedical Engineering*, *13*(6), 429–438.
16. Zavarise, G., & Wriggers, P. (2000). Contact with friction between beams in 3-D space. *International Journal for Numerical Methods in Engineering*, *49*(8), 977–1006.
17. Litewka, P., & Wriggers, P. (2002). Contact between 3D beams with rectangular cross-sections. *International Journal for Numerical Methods in Engineering*, *53*(9), 2019–2041.
18. Litewka, P., & Wriggers, P. (2002). Frictional contact between 3D beams. *Computational Mechanics*, *28*(1), 26–39.
19. Konyukhov, A., & Schweizerhof, K. (2010). Geometrically exact covariant approach for contact between curves. *Computer Methods in Applied Mechanics and Engineering*, *199*(37–40), 2510–2531.

20. Neto, A. G., Pimenta, P. M., & Wriggers, P. (2016). A master-surface to master-surface formulation for beam to beam contact. Part I: Frictionless interaction. *Computer Methods in Applied Mechanics and Engineering*, 303, 400–429.
21. Neto, A. G., Pimenta, P. M., & Wriggers, P. (2017). A master-surface to master-surface formulation for beam to beam contact. Part II: Frictional interaction. *Computer Methods in Applied Mechanics and Engineering*, 319, 146–174.
22. Durville, D. (2012). Contact-friction modeling within elastic beam assemblies: An application to knot tightening. *Computational Mechanics*, 49(6), 687–707.
23. Bussolati, F. (2019). *Multi-scale model of the fatigue of mooring wire ropes for floating offshore wind turbines* (Doctoral thesis). Université Paris-Saclay.
24. Guidault, P. A., Bussolati, F., Guiton, M., Allix, O. (2019). A small-sliding node-to-node formulation for beam-to-beam frictional contact with large displacements. In *VI International Conference on Computational Contact Mechanics*.
25. Bussolati, F., Guiton, M., Guidault, P. A., Poirette, Y., Martinez, M., & Allix, O. (2019.) A new fully-detailed finite element of spiral strand wire ropes for fatigue life estimate of a mooring line. In *ASME 2019 38th International Conference on Ocean, Offshore and Arctic Engineering*. American Society of Mechanical Engineers.
26. Raoof, M. (1992). Free bending fatigue of axially pre-loaded spiral strands. *The Journal of Strain Analysis for Engineering Design*, 27(3), 127–136.
27. Jonkman, J., Butterfield, S., Musial, W., Scott, G. (2009). Definition of a 5-MW reference wind turbine for offshore system development. National Renewable Energy Laboratory, Golden, CO, Technical Report No. NREL/TP-500-38060.
28. Hasselmann, K., Barnett, T., Bouws, E., Carlson, H., Cartwright, D., Enke, K., et al. (1973). Measurements of wind-wave growth and swell decay during the joint north sea wave project (JONSWAP). *Ergänzungsheft*, 8–12.
29. Nath, J. H., & Ramsey, F. L. (1976). Probability distributions of breaking wave heights emphasizing the utilization of the JONSWAP spectrum. *Journal of Physical Oceanography*, 6(3), 316–323.
30. Kim, H., & Kim, M. (2016). Comparison of simulated platform dynamics in steady/dynamic winds and irregular waves for OC4 semi-submersible 5MW wind-turbine against DeepCWind model-test results. *Ocean System Engineering*, 6(1), 1–21.
31. Fargues, J.-P. (1995). *Modélisation dynamique des risers pétroliers en grands déplacements* (Doctoral thesis). École Centrale de Paris.
32. Fontaine, E., Heurtier, J., Durville, D., Toumit, S., & Prat, C. (2002). Modeling of riser contact-friction problems. In *Offshore Technology Conference*.
33. Hall, M. T. J. (2013). *Mooring line modelling and design optimization of floating offshore wind turbines* (Master thesis). University of Victoria.
34. Molin, B. (2002). *Hydrodynamique des structures offshore*. Editions Technip.
35. Perier, V. (2010). *Etude de l'influence des conditions environnementales sur le comportement en fretting, fatigue et fretting-fatigue des câbles du génie civil* (Doctoral thesis). École Centrale de Lyon.
36. Siegert, D. (1997). *Mécanismes de fatigue de contact dans les câbles de haubanage du génie civil* (Doctoral thesis). École Centrale de Nantes.